Satoh *et al. Earth, Planets and Space* (2016) 68:74
DOI 10.1186/s40623-016-0451-z

Earth, Planets and Space

FULL PAPER Open Access

Development and in-flight calibration of IR2: 2-μm camera onboard Japan's Venus orbiter, Akatsuki

Takehiko Satoh[1,2*], Masato Nakamura[1†], Munetaka Ueno[1†], Kazunori Uemizu[3†], Makoto Suzuki[1], Takeshi Imamura[1], Yasumasa Kasaba[4], Seiji Yoshida[5†] and Masafumi Kimata[6]

Abstract

IR2, a near-infrared camera in the 2-μm region onboard Akatsuki has been developed to primarily study the middle-to-lower atmospheric dynamics of Venus as probed in the 1.74- and 2.3-μm "windows" of the CO_2 atmosphere on the night side. The spatial and temporal variability of CO below the clouds is also studied by differentiating 2.32-μm CO-band images from simultaneous 2.26-μm images. Images of the night-side disk in these wavelengths will enable us to determine the zonal and meridional winds near the cloud-base altitudes. IR2 also images at 2.02 μm, the center of a CO_2 absorption band. Such images can visualize the variation of the cloud-top altitudes as contrast features due to different absorption path lengths of the reflected sunlight. Tracking of the 2.02-μm features will also enable us to obtain wind information at the cloud-top level. Together with the other cameras and the radio science equipment on Akatsuki, IR2 will contribute to understanding of the production and maintenance mechanism of super-rotation in the Venusian atmosphere. During cruise, IR2 observed zodiacal light with a broad-band H filter (1.65 μm), imaged the Earth–moon remotely from a distance of ~30 million km, and determined Venus's phase curves at small phase angles. We have just started the early phase operation check of IR2 at Venus, as the orbit insertion in December 2015 was successful.

Keywords: Venus, Atmosphere, Near-infrared, Atmospheric windows, Imaging camera, Dynamics, Clouds, Zodiacal light

Introduction

After nine orbital revolutions around the sun in five Earth years (Nakamura et al. 2011), Japan's Venus orbiter finally arrived at Venus on December 7, 2015 (Nakamura et al. 2016). The 2015 orbit insertion (VOI-R1) was realized with attitude-control thrusters, as the main engine was broken, owing to a clogged check valve of the fuel pressure system, which occurred in the 2010 VOI attempt. Although the new orbit of Akatsuki is highly elongated, it is retrograde (or westward) and near-equatorial (Nakamura et al. 2014) so that a large portion of the original science objectives (Nakamura et al. 2011) may still be achieved.

IR2, the 2-μm camera, is intended to study the meteorology of Venus by utilizing near-infrared (NIR) "windows" of the CO_2 atmosphere discovered in 1983 (Allen and Crawford 1984). Contrast features at 1.74 and 2.3 μm on the night-side disk are the silhouette of spatially inhomogeneous scatterers/absorbers, back-illuminated by the glow of the hot (300–500 K) lower atmosphere (Kamp and Taylor 1990). Spatially resolved maps in these windows were acquired by space instruments, such as Near-Infrared Mapping Spectrometer (NIMS) on Galileo (February 1990 flyby) (Carlson et al. 1993) and Visible, Infrared and Thermal Imaging Spectrometer (VIRTIS) (Drossart 2007; Piccioni 2007) on Venus Express (in orbit from 2006 to 2015) (Svedhem et al. 2009; Titov et al. 2009). Opacity inhomogeneities due to particles with radius >3 μm at

*Correspondence: satoh@stp.isas.jaxa.jp
†Masato Nakamura, Munetaka Ueno, Kazunori Uemizu, and Seiji Yoshida are equal contributors
[1] Institute of Space and Astronautical Science, Japan Aerospace Exploration Agency, 3-1-1 Yoshinodai, Chuo-ku, Sagamihara 252-5210, Japan
Full list of author information is available at the end of the article

or near the cloud base (48–50 km altitudes) are believed to be responsible for such silhouettes (Grinspoon et al. 1993), being consistent with the fact that they move at speeds lower than those at the cloud top (Sánchez-Lavega et al. 2008). Accumulated data in these NIR windows have proved their usefulness in inferring the conditions in the middle-to-lower atmosphere (Carlson et al. 1993; Taylor and Crisp 1997; Grinspoon et al. 1993; Satoh et al. 2009; Tsang et al. 2008; Wilson et al. 2008).

IR2, one of the key instruments onboard Akatsuki, is intended to image Venus in these NIR windows. In this paper, we describe the science objectives, instrumentation, in-flight calibration, and expected performance of IR2 in the Venus orbit.

Science objectives

Akatsuki is a multi-band imaging mission equipped with four imaging cameras, from 0.283 to 10 μm, with 12 discrete filters, plus a special high-speed sensor with four filters exclusively for lightning and airglow measurements. The science objectives of the mission are described in the mission overview (Nakamura et al. 2011). The main role of IR2 is to probe the middle-to-lower atmosphere for dynamics, aerosols, and trace gases, by utilizing the NIR spectral transparency "windows."

IR2 is designed such that it satisfies the following scientific requirements. The hardware components of IR2 are summarized in Table 1, and the system block diagram is presented in Fig. 1. The filter characteristics are summarized in Table 2 and Fig. 2.

Atmospheric dynamics

To understand the production and maintenance mechanisms of super-rotation on Venus, it is essential to quantitatively characterize the atmospheric motions in 4-D space (3 spatial plus 1 temporal). Previous entry probe missions acquired mainly 1-D (vertical) profiles, in which westward zonal winds increase from ~0 at the ground to ~100 m/s near the cloud top (~70 km) (Schubert 1983). For the cloud-top region, another dimension, the "temporal" variability, was studied using VEX/VMC data (Moissl et al. 2009; Kouyama et al. 2013). While Moissl et al. indicated short-term variability of day scale, Kouyama et al. suggested longer and periodic changes of zonal wind velocity with an amplitude of ~20 m/s and a timescale of a few hundred days. Other periodicities are suggested by Khatuntsev et al. (2013) and by Patsaeva et al. (2015). At altitudes of 1.74- or 2.3-μm opacity sources (~48–50 km) (Grinspoon 1993), the velocity is ~60 m/s with substantial variability (Sánchez-Lavega et al. 2008), although a periodicity similar to that at the cloud top has not yet been detected. Investigating such, to enhance our knowledge about the atmospheric motions in 4-D, will certainly be the most important mission of IR2.

VEX/VIRTIS-M images revealed numerous mesoscale waves in the upper and lower atmosphere (Peralta et al. 2008), confined to poleward of 40°S. Because of VEX's polar orbit, however, detection of waves might have been biased to higher southern latitudes. IR2, from an equatorial orbit, complements the VEX/VIRTIS-M observations, as it will allow a more intensive search for

Table 1 Components of IR2

Component	Sub-component	T^a	Weight (g)	Power consumption and remarks
IR2-CMR	IR2-SNS		1100	5.0 W (from IR-AE, when imaging)
	(17-μm pitch 1M pix. PtSi)	66		IFOV = 0.20 mRad/FOV = 12°
	IR2-OPT (triplet lens)	172		f = 84.6 mm (170 K), F / 4
	IR2-STR (structure)	–		
	IR2-FWH (filter wheel)	172		7.2 W (from IR-AE, when in motion)
	IR2-FLTR	83		Fixed short-wavelength pass filter
	IR2-ELC		250	A set of wire herness
IR2-THRM	CP (Radiator plate)		2500	AlBeMet162 alloy metal
	IR2-CMP (compressor)		3500	50 W (from IR2-CDE)
	IR2-CHD (cold head)		800	
IR2-CDE			3600	74.4 W (50 W to IR2-CMP)
IR2-H			2320	Box-shape baffle
IR-AE			3300	40.4 W (when imaging)
				33.4 W (when FWH in motion)
	IR-AE-WHN		200	A set of wire herness
Total			17,570	114.8 W (when imaging)
				107.8 W (when FWH in motion)

[a] Temperatures of IR2-CMR estimated for the most severe ambient condition in Venus orbit

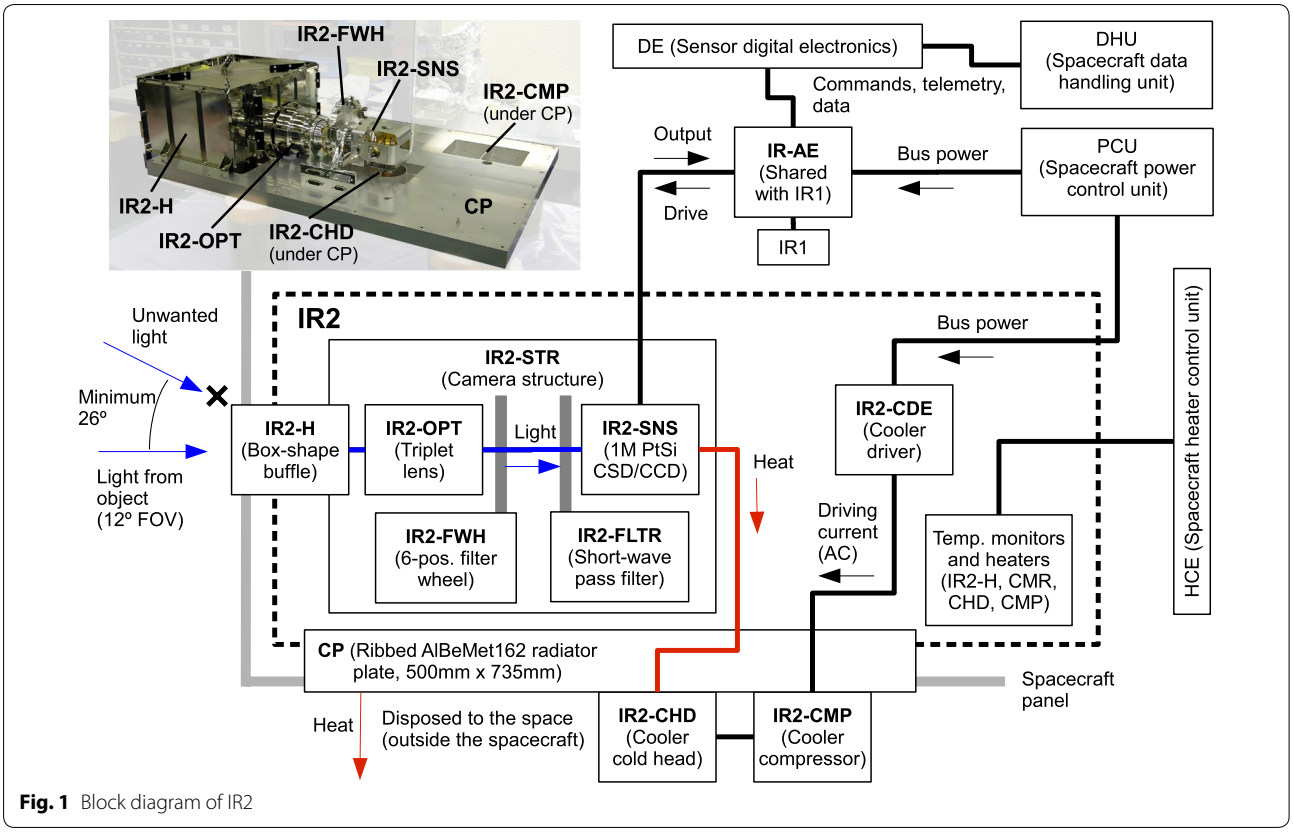

Fig. 1 Block diagram of IR2

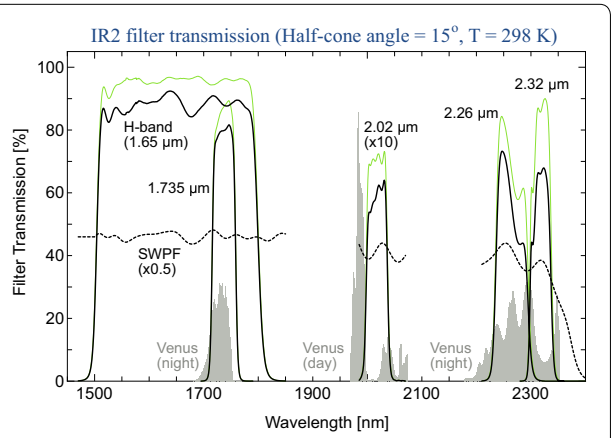

Fig. 2 IR2 filter transmissions: Curves in *black* are the products of individual filters and IR2-FLTR (short-wavelength pass), while curves in green are without IR2-FLTR. The curve for IR2-FLTR is shown with *dashed lines*. Curves will shift by ~−2 nm at operating temperatures. Shown in shades are typical Venus spectra for 1.74- (night), 2.02- (day), and 2.3-μm (night) wavelength regions in arbitrary scales

such waves at low latitudes than was possible with VEX. Together with the previous data, IR2 will allow us to better understand the origins and roles of these waves.

CO as a tracer of atmospheric circulation

CO is thought to be a good tracer of the atmospheric circulation. After photochemical production in the upper atmosphere via CO_2 photodissociation (von Zahn et al. 1983),

$$CO_2 + h\nu \rightarrow CO + O \tag{1}$$

CO will be transported poleward by the Hadley cell and descend to the lower atmosphere. Grassi et al. (2014) suggested that the region of maximum [CO] above the clouds (60°S), as retrieved from VEX/VIRTIS-M spectra, is consistent with such circulation. Once in the lower atmosphere, CO, while transported, thermodynamically equilibrates with other gases and aerosols (Yung et al. 2009). Therefore, mapping and long-term monitoring of sub-cloud CO will yield valuable information about the meridional circulation. While the volume mixing ratio of sub-cloud CO is believed to be nearly constant for the altitudes from 0 to 50 km, the CO absorption band at 2.32 μm is most sensitive to the CO abundance at a ~35 km altitude. Previous studies show more CO (~40 ppmv) at high latitudes than near the equator (~25 ppmv), suggestive of equatorward transport of CO (Taylor and Crisp 1997; Tsang et al. 2008). IR2 allows differential

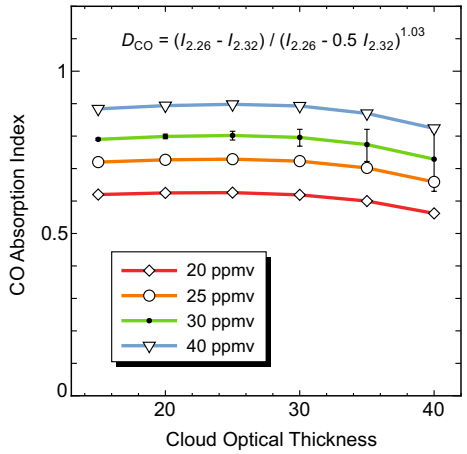

Fig. 3 CO absorption index: The CO absorption index defined in Eq. (2) is plotted for various sub-cloud CO abundances against the opacity of underlying cloud. The 30-ppmv curve has error bars estimated by applying $\pm 1\sigma$ to both $I_{2.26\,\mu m}$ and $I_{2.32\,\mu m}$. It is found that these indices are stable up to cloud opacities ~30

photometry of CO absorption by acquiring 2.26-μm (free of CO absorption) and 2.32-μm (with CO absorption) images. We define the CO absorption index in the following form:

$$D_{\mathrm{CO}} = (I_{2.26\mu\mathrm{m}} - I_{2.32\mu\mathrm{m}})/(I_{2.26\mu\mathrm{m}} - \alpha\, I_{2.32\mu\mathrm{m}})^{\beta} \quad (2)$$

($I_{2.26\mu m}$: radiance at 2.26 μm, $I_{2.32\mu m}$: radiance at 2.32 μm, and α and β are constants). Such a quantity is expected to be less affected by uncertainties of radiometric calibration. We have found a combination of $(\alpha, \beta) = (0.5, 1.03)$ renders D_{CO} nearly independent of overlaying cloud opacities up to 30 (Fig. 3). We will derive pixel-by-pixel maps of CO absorption indices to study the hypothetical return flow of the Hadley cell (or indirect cell) (Schubert 1983), which may not be detected by cloud tracking results.

Cloud-top altimetry

Haus et al. (2014) performed a comprehensive study of mesospheric temperature and cloud parameters while demonstrating usefulness of analyzing multi-window (1.74-, 2.3-, and 4.3-μm) spectra of the Venus night-side disk (VEX/VIRTIS-M). On Akatsuki, longwave infrared camera (LIR) can replace 4.3-μm observations by mapping the cloud-top temperatures at 8–12 μm (Fukuhara et al. 2011), while IR2 provides 1.74- and 2.3-μm cloud opacity data. IR2 also measures the cloud-top altitudes by imaging the sunlit side of Venus in the CO_2 absorption band (2.02 μm).

In the CO_2 absorption band, the reflected sunlight is attenuated by a factor proportional to the column abundance of CO_2 at the cloud top. Therefore, if the cloud albedo and the cloud-top structure are spatially uniform, contrast features at 2.02 μm reflect the undulation of the cloud top. Such cloud-top altimetry has been performed using VEX/VIRTIS-M data (Ignatiev et al. 2009) in a different CO_2 band (1.6 μm), revealing stable cloud-top altitudes of 74 km at latitudes up to ~ 50° and lower (63–69 km) in the polar regions.

The sensitivity of the 2.02-μm images to various cloud-top altitudes is examined in Fig. 4. A simple reflecting surface is located at $Z_{RS} = 72$, 70, and 68 km altitudes to indicate how much contrast we expect to see in the 2.02-μm images. An additional curve is for a model with a diffuse aerosol layer (2-km thick) added on top the reflecting surface at 70 km. This demonstrates how limb-darkening curves change according to the cloud-top structure. Because IR2 almost always takes full-disk Venus images, the limb-darkening curves enable determination of the typical structure at the cloud-top level and then local contrasts can be interpreted as the undulations.

UVI, LIR, and IR2 altogether provide the cloud-top dynamics, temperatures, and altitude data with which we investigate transportation of energy and materials in the upper cloud layer. Ground-based observations of cloud-top temperatures, as demonstrated with Subaru/COMICS (Sato et al. 2014), may also be combined.

Aerosol properties

The Venus cloud layer has an enormous vertical extent, from its top at ~70 km to the bottom at ~50 km with a few distinctive layers within it (Knollenberg and Hunten 1980; Esposito et al. 1983). Studying the properties of aerosols will tell us how they are produced and maintained in the atmosphere. Based on the analysis of Galileo/NIMS data, the following empirical formula has been proposed to describe the cloud size parameters (Carlson et al. 1993):

$$m = (I_{1.74\mu\mathrm{m}})/(I_{2.3\mu\mathrm{m}})^{0.53} \quad (3)$$

(m: size parameter, $I_{1.74\mu m}$: radiance at 1.74 μm, $I_{2.3\mu m}$: radiance at 2.3 μm). This simple yet useful formula has been used as a convenient tool to classify the clouds of different particle sizes (Carlson et al. 1993; Wilson et al. 2008). Carlson et al. identified five branches of m parameter in Galileo/NIMS data and interpreted them as variations in mixing ratio of two distinctive modes of particles (one is ~3 μm and another is ~7 μm in diameter).

Cloud condensation depends on local conditions (temperature, vapor pressure, motion of air parcels, existence of condensation nuclei, etc.) that may not be understood with snapshot data. Statistical analysis is therefore essential (Carlson et al. 1993; Wilson et al. 2008). IR2 will provide spatially resolved 1.74- and 2.3-μm images

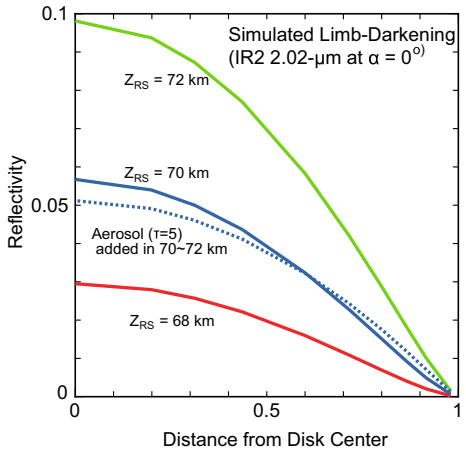

Fig. 4 Limb-darkening curves at 2.02 μm: Sensitivity of cloud-top altimetry in the 2.02-μm filter is demonstrated. Three model curves with the reflecting surface (RS) at 68, 70, and 72 km altitudes are shown. Also shown with *dashed line* is the 70-km RS model but with aerosols ($\tau = 5$) uniformly mixed in the 70–72 km layer. This shows the effectiveness of limb-darkening analysis to infer the cloud-top structures

Table 2 Filters on IR2

Wavelength		Ave. trans.[a] (%)	Day or night	Scientific targets
Center (μm)	Width (μm)			
1.735	0.043	81	N	Dynamics and clouds
2.260	0.058	60	N	Dynamics and clouds
2.320	0.038	62	N	CO distribution
2.020	0.040	6.0	D	Cloud-top altimetry
1.650	0.300	88	–	Zodiacal light

[a] Integrated transmission divided by the band width (see text)

continuously from a retrograde and near-equatorial orbit to allow statistical studies.

Interplanetary dust

IR2 studies the distribution of interplanetary dust in the 0.7–1.0 AU region from the Sun by observing the zodiacal light at 1.65 μm (astronomical H-band). Sensitivity is required to detect the typical flux of $\sim 4 \times 10^{-7}$ (W m^{-2} sr^{-1}) in the H-band (Matsumoto et al. 1996). The results of observations are discussed in a later section.

Instrumentation

Detector (IR2-SNS) and electronics (IR-AE)

IR2 utilizes a platinum silicide (PtSi) Schottky-barrier (SB) detector. The characteristics of IR2-SNS are as follows:

- Although quantum efficiency (QE) is not high, ~4 % at 2 μm, the uniformity and stability of PtSi SB are superb owing to its monolithic structure (Akiyama et al. 1994). For applications in which shot noise of incoming photon dominates (e.g., Venus observations), the advantage of PtSi overcomes the disadvantage of low QE. Domestic availability of large format arrays was another major reason why the PtSi SB was chosen for IR2. The IR2-SNS (a 1-Mpixels PtSi SB detector), manufactured by Mitsubishi Electric, Corp. (MELCO), has all design details disclosed to us.
- On 1040 × 1040 pixels (17-μm pitch) of IR2-SNS, the PtSi SB covers the middle 1024 × 1024 pixels, leaving 8 lines around the imaging area not sensitive to IR. Such non-sensitive pixels are used to precisely calibrate the zero level for low-signal observations. Pixels of IR2-SNS are read through the CSD(charge sweep device)/CCD architecture identical to the Si CSD/CCD of IR1 (Iwagami et al. 2011). Because the CSD channel (vertical in the sensor) holds electrons only from a single pixel at a time, it can be very narrow (Akiyama et al. 1994), contributing to a good fill factor, ~59 %, without microlenses.
- The current density in PtSi, J [A m^{-2}], due to thermal electrons, is governed by the following Richardson's equation:

$$J = AT^2 \exp[-\phi_b e/kT] \tag{4}$$

(T: temperature, ϕ_b: barrier height, e: elementary charge, k: Boltzmann constant, and A: Richardson constant, 1.20173×10^6 [A m^{-2} K^{-2}]). The barrier height, ϕ_b, of IR2-SNS is ~0.197 (eV) which yields thermal electrons at a rate of 135, 2960, and 4.2×10^4 (s^{-1} pix^{-1}) at $T_{\mathrm{SNS}} = 60$, 65, and 70 K, respectively. Since the full well is approximately 10^6 electrons per pixel, the dark current saturates a pixel in a few tens of seconds at $T_{\mathrm{SNS}} = 70$ K. Therefore, the sensor needs to be cooled to below 70 K with stability ($\Delta T < 1$ K/h).

IR2 and IR1 (Iwagami et al. 2011) are controlled by IR-AE (Fig. 1). The output from the sensor is digitized at 14-bit depth with one count corresponding to 70 electrons. The full well is, therefore, 14,000 counts, just under the largest 14-bit integer.

Filters (IR2-FWH/FLTR) and optics (IR2-OPT)

A 6-position filter wheel (IR2-FWH), of which one is for dark current measurements, holds five observing filters selected by referring to the science objectives and typical spectrum of Venus (Fig. 2). IR2-FWH/FLTR/OPT are all cooled to suppress the radiation (Table 1).

- Two prominent NIR windows, the primary target of IR2, are probed with filters at 1.735 and 2.26 μm, with respective band widths of 0.043 and 0.058 μm.
- To map the distribution of sub-cloud CO, the absorption band at ∼2.32 μm is chosen. This will be differentiated with 2.26 μm (free of CO absorption) to evaluate the CO absorption index (Eq. (3); Fig. 3).
- For the cloud-top altimetry, we have chosen 2.02 μm, center of a strong CO_2 absorption band (Fig. 4).
- The last filter is an astronomical H-band (1.65 μm). This broad-band filter is dedicated to the zodiacal light observations.

A blocking filter (IR2-FLTR), a short-wavelength pass filter (SWPF) which effectively blocks unwanted infrared radiation, $\lambda > 2.46\,\mu$m, is fixed in front of IR2-SNS. Note that the "Ave. trans." in Table 2 are calculated with the following equation:

$$\bar{R} = \int_{\lambda 1}^{\lambda 2} R(\lambda)\mathrm{d}\lambda \,/\, \mathrm{b.w.} \tag{5}$$

($\bar{R}$: average transmission, λ: wavelength, $R(\lambda)$: transmission as a function of λ, $[\lambda 1 : \lambda 2]$: region of integral, b.w.: band width given in Table 2).

The IR2 optics (IR2-OPT) is a triplet type ($F = 4$) in Fig. 5, with the following characteristics.

- With a focal length of 84.2 mm, IR2-OPT yields a field of view (FOV) of 12° × 12°. The IFOV is 0.20 mRad (Table 1). In order to reduce difficulty of optical alignment in developing phases, while increasing robustness, IR2-OPT employs a rather simple design: a triplet of ZnS (G1), quartz (G2), and quartz (G3). Geometrical distortion is well corrected, and this was confirmed with star-field images during the cruise (described in a later section).
- The optics is designed so as to achieve diffraction-limited spatial resolution at $\lambda = 1.735$, 2.02, 2.26, and 2.32 μm. The modulation transfer function (MTF) for the Nyquist frequency (30 lines per mm) is ∼0.65 at 2.32 μm and is better at other three wavelengths. IR2-OPT maintains MTF >0.5 within ±80 μm of defocusing. As IR2 defocuses at a rate of 4.5 μm/K, as T_{OPT} changes, good optical performance is expected for T_{OPT} range of ±18 K. The low-temperature focal length is 84.6 mm at 170 K (Table 1).
- In order to use the triplet type, we relaxed the requirement for chromatic aberration correction and allowed slight focus shifts for different filters. The best focus positions (170 K), relative to that at 1.735 μm, are +76.7 μm at 2.02 μm, +7.0 μm at 2.26 μm, and −20.6 μm at 2.32 μm, respectively. To compensate for the large focus shift at 2.02 μm, the 2.02-μm filter was made thinner by 100 μm.
- The chromatic aberration becomes more noticeable for the H-band (1.65 μm): The relative focus is −60 μm and the MTF >0.45 across 80 % of the FOV. The H-band images are, however, primarily used to study the large-scale features of the zodiacal light, so the highest spatial resolution is not required. We therefore decided not to correct the chromatic aberration in the H-band, but to 2 × 2 bin the H-band images on board.

IR2-THRM and IR2-CDE: thermal control

IR2-SNS needs to be cooled to ∼65 K, and IR2-OPT/FWH/FLTR to $T < 195$, 180, and 85 K, respectively. To achieve these, a single-stage Stirling-cycle cryocooler is employed. The cooler, manufactured by Sumitomo Heavy Industries, Ltd., has heritage from previous Japanese space missions (Hasebe et al. 2008), with reliability and long lifetime (>50,000 h on the laboratory test model). When IR2-CMP is driven at 50-W power by IR2-CDE, 1.3 W of heat is continuously removed from an object at the cold tip (at 60 K) of IR2-CHD. The 50,000-h (or longer) lifetime of the cryocooler would allow ∼2000 Earth days of continuous cooling of IR2. However, to survive the severe thermal condition in the Venus orbit, we plan to lower the power or even to switch off the cooler when it is appropriate (long-duration umbra passages, for example). The cold tip is in contact, via a flexible thermal path of copper, to the detector housing, achieving the required cooling of IR2-SNS. IR2-FLTR, directly mounted on the detector housing, is cooled together with IR2-SNS. The thermal coupling of the detector housing to IR2-OPT/FWH is optimized such that the optics are also cooled to the desired temperatures (<195 K). Actually, ∼90 % of the heat removed by the cold tip comes from IR2-OPT/FWH. Estimated operating temperatures are shown in Table 1.

To efficiently dispose of the heat from IR2-CMP and IR2-CHD by utilizing the entire surface of radiator (CP), the material needs to be of high heat conductivity. By using a large, 500 mm (W) × 735 mm (D), ribbed plate of AlBeMet162 (aluminum–beryllium alloy metal), the desired thermal control of IR2 is achieved.

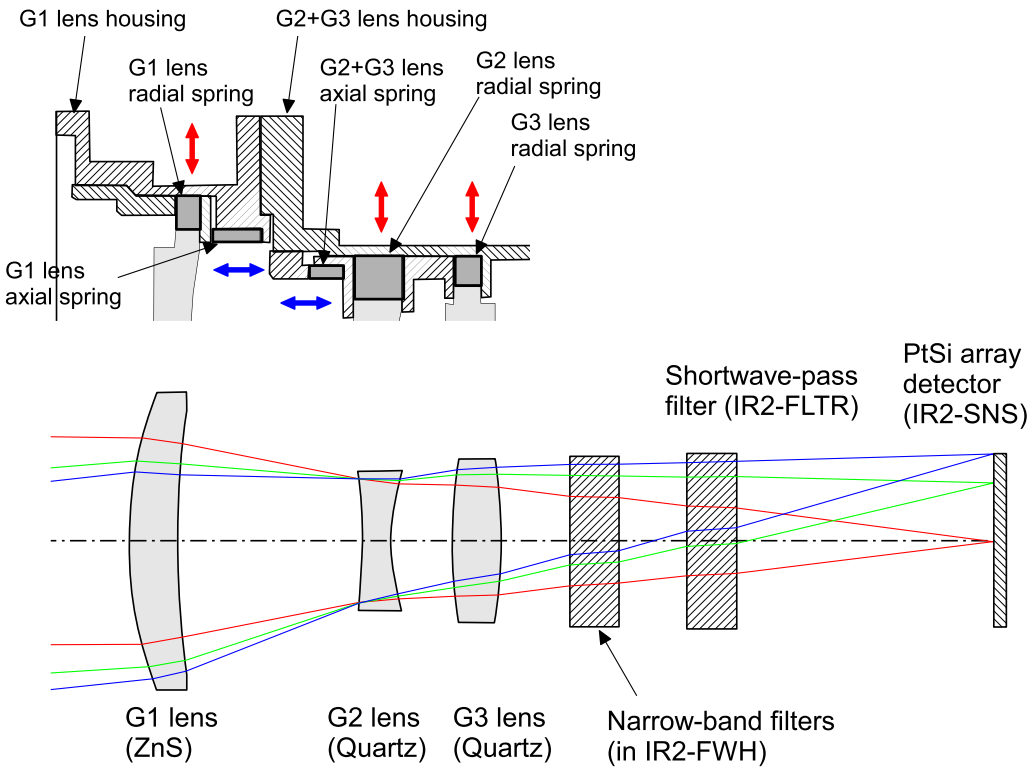

Fig. 5 IR2 optics and the holder: a triplet optics of IR2. To lessen excessive stresses between metal and glass at low temperatures, while tolerating the harshest environment of launch, "slitted" spacers in both radial and axial directions are used to hold and align the lenses

IR2-STR: alignment of cooled optics

IR2 tolerated the harsh environment of the launch by employing a special mechanism for its optics. Because the cryocooler was off, IR2 was at the ambient temperature at the time of launch. A lens mount, if too loose, may fail to survive the launch. On the contrary, a lens mount, if too tight, could yield excessive stress to the glass lens, when cooled to $T_{\mathrm{OPT}} < 195$ K in the space, risking damage to the lens.

We have developed a lens-holding mechanism with "slitted" spacer rings placed axially and radially (Fig. 5) to absorb differential thermal expansion (shrinkage) of glass and metal. The biggest advantage of this mechanism is the reproducibility of the optical alignment. Tests with a prototype model have proved that this mechanism would maintain relative positions of lens elements at an accuracy of 10–20 μm. By statistically adding such errors to ray tracing simulations, the probability of achieving MTF >0.5 is reasonably high. During the focus adjustment of the flight model, sharp spot images were repeatedly obtained and the mechanism's good reproducibility has been confirmed.

The actual images were acquired in space, and the performance of this mechanism was confirmed. This is described in the following section.

Photometric characteristics of IR2

A set of "flat-field" data was obtained in the laboratory. The flight model of IR2, including IR2-CMR, IR2-CHD, and IR2-CMP, is placed in a vacuum chamber. The chamber has a viewing port (a quartz window) which faces to the window of the laboratory. We use a diffuser to further flatten the incident light. The flat-field correction on an example 1.735-μm image is demonstrated in Fig. 6. The gain variation between the four quadrants is canceled out to a level that the brightness discontinuity between the adjacent quadrants disappears.

In-flight calibration

While in space, we have acquired three datasets that were used for the photometric calibration of IR2:

A Imaging of star fields: October 22–23, 2010, at 1.65 μm in the high-gain mode (10 times more sensitive than the normal gain) and 122.8-s integration.
B Imaging of the Earth and the moon: October 26, 2010, at 2.02 μm (normal gain and 6.97-s integration).
C Disk-integrated photometry of Venus: February–March 2011 at 2.02 μm (normal gain and 6.97-s integration) (Satoh et al. 2015).

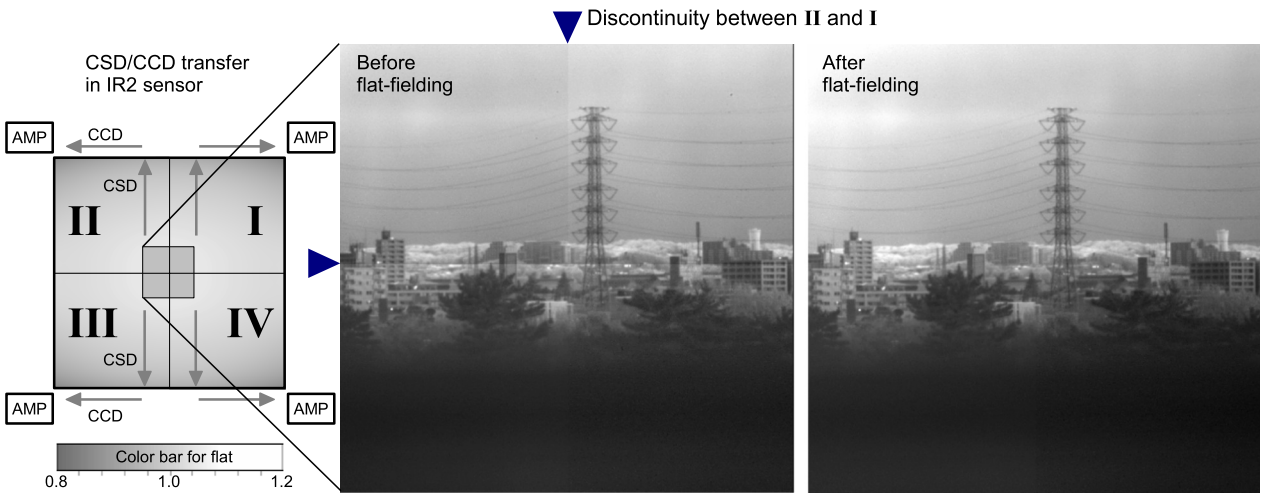

Fig. 6 Flat-field correction: Flat-field correction is applied to an example 1.735-μm image. The brightness discontinuity between adjacent quadrants disappears, indicating appropriateness of the correction. The overall flat-field pattern is indicated in the left with explanation how pixels are read with CSD/CCD architecture. The gray scale from 0.8 to 1.2 is shown as indicated in the *color bar*

Dataset **A** is a full-longitude scan of the ecliptic plane to study zodiacal light in the H-band. The results of aperture photometry on seven stars of Pleiades are compared with the published H-band magnitudes (Stauffer 2007), and it is found that a 3.68 H-band magnitude star would yield 10,000 counts (Fig. 7). This compares favorably to the estimated sensitivity, based on design parameters of IR2, which expects 10,000 counts for a 3.28 H-band magnitude star. A small difference (~13 %) may be attributed to ripples in the filter transmission, to the quantum efficiency (measured using a different sensor), and to uncertainties in the star brightness.

It should be mentioned that dataset **A** was rather noisy, due to insufficient cooling of the sensor (59 K at its best), to detect the zodiacal light of which typical flux is $\sim 4 \times 10^{-7}$ (W m^{-2} sr^{-1}). Considering the IFOV of 0.20 mRad, 6.4×10^{-14} (W m^{-2}) is expected to fall in one 2×2-binned pixel. This translates to ~10 counts in the 122.8-s integrated image and may well be masked by the noise at the level of tens of counts.

Dataset **C** was converted to Venus albedos by correcting for the radii and distances with dataset **B** as a reference (Satoh et al. 2015), but neither was treated as absolute radiance. At the time of acquisition of **B**, the absolute flux from the moon at Akatsuki is estimated to be 2.5×10^{-12} (W cm^{-2} μm^{-1}) for the conditions given in Satoh et al. (2015). Based on the IR2 design parameters, this translates to an expectation of 475 counts which agrees very well with the actual measurement, 477 counts. The calibration coefficients, including results from **A** and **B**, are summarized in Table 3.

Using a star-field image of **A**, astrometry is performed. As is mentioned in the above, the image was 2×2 binned on board. In the 12° squared FOV, we measured the position of 5 stars: Maia (star (2) in Fig. 7), ϵ Tau, 36A and 37A Tau, and BD+16 560. We used the *ccmap* task in IRAF (Image Reduction and Analysis Facility) to locate the centroid of each star and fit their celestial coordinates. The obtained plate scale is 82.12 (arcsec pix^{-1}) in X and 82.10 (arcsec pix^{-1}) in Y with rms residuals of 13.2 arcsec in X and 8.9 arcsec in Y. This implies that the focal length is 85.42 mm, or +1.0 % of the designed value (84.6 mm at 170 K). Since the fitting residual is ~1/6 pixel, it is confirmed that the geometrical distortion of IR2 is negligibly small.

Current condition and expected performance after VOI

Condition of thermal protection system (TPS)

Deterioration of TPS has been monitored as temperatures of IR2 components exposed to space (IR2-CMP/CHD) have increased. Temperature rises of ~5 °C were noticed by the 9th perihelion passage (August 2015). Absorption coefficients and emissivities in numerical thermal model are updated to reproduce such changes. With the updated numerical model, the effectiveness of TPS is assured such that the desired cooling of IR2 would likely be achieved in the Venus orbit.

Effects of the "new" orbit

Although Akatsuki's new orbit after the 2015 VOI is retrograde, and near-equatorial as originally planned, it is highly elongated with apoapsis altitudes of ~0.4 million km. In one orbital revolution, the spacecraft is in

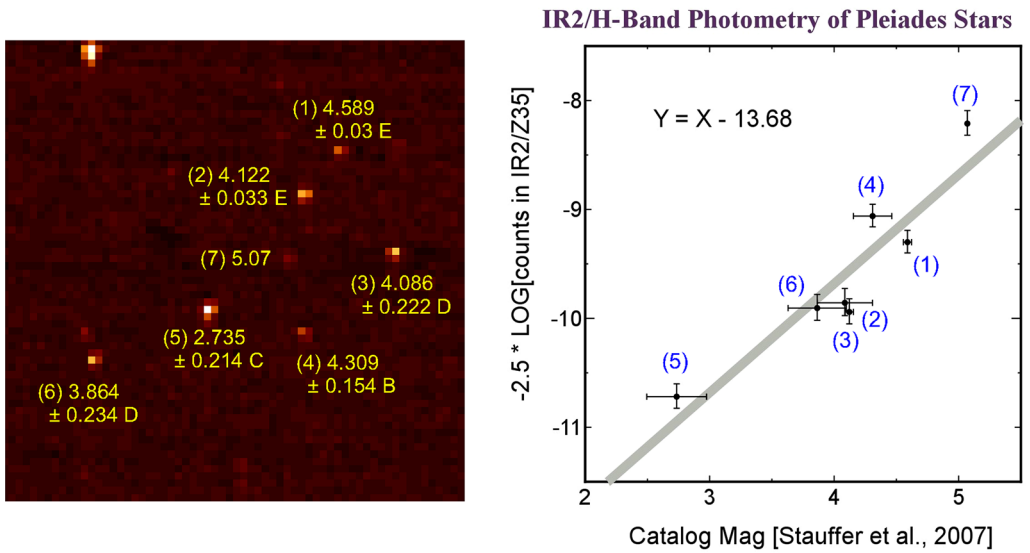

Fig. 7 H-band photometry of Pleiades Aperture photometry is performed on seven stars in Pleiades. By referring to published star magnitudes, the relationship between the star magnitudes and IR2 counts is obtained. A 3.68 H-band magnitude star would yield 10,000 IR2 counts (high-gain mode)

Table 3 Calibration coefficients

Wavelength (μm)	Q.E. (%)	Calib. coefficients. ($J\ cm^{-2}\ \mu m^{-1}\ ADU^{-1}$)	Flags
1.735	5.2	2.6×10^{-15}	E
2.260	3.9	2.6×10^{-15}	E
2.320	3.8	3.8×10^{-15}	E
2.020	4.5	3.7×10^{-14}	C
1.650	4.6	4.0×10^{-17}	C,H

E estimated, *C* in-flight calibrated, *H* high-gain mode

the "closest" distance range (0–0.1 million km) for 19 h, in the "close" range (0.1–0.2 million km) for 36 h, in the "middle" range (0.2–0.3 million km) for 63 h, and in the "far" range (0.3–0.4 million km) for 167 h (Nakamura et al. 2014). This no longer allows the spacecraft motion to be synchronized to the super-rotating atmosphere and affects the longitudinal coverage and the spatial resolution of images.

The "closest" distance range (0–0.1 million km)

In this distance range, the highest spatial-resolution images (~20 km per pixel from 0.1 million km) are acquired to study the dynamics and morphology of the clouds. To obtain a series of images of the same cloud features from around the periapsis, so-called profiled attitude control of the spacecraft will be used. The data in this distance range would produce the finest wind vectors to study the production and maintenance mechanisms of super-rotation.

The "close" distance range (0.1–0.2 million km)

Studies similar to the "closest" distance range are planned for this range. Although the spatial resolution is decreasing (~40 km per pixel from 0.2 million km), longer cloud tracking is possible as the orbital motion slows down. To remove the spiky noise of cosmic-ray origin, we take three successive images in the same filter and take a median of them at this distance range or farther. Required stability of spacecraft attitude control, better than 1 pixel while taking three images, has been confirmed during the initial test phase in the Venus orbit.

The "middle" distance range (0.2–0.3 million km)

The spatial resolution gets even lower (~60 km per pixel from 0.3 million km). Since the diameter of Venus in the image from this range is ~200 pixels, we no longer have to receive the full 1024 × 1024-pixel frames from the spacecraft. A "region of interest (ROI)" function of the data recorder allows an arbitrary sub-frame of the image to be recorded. We plan to record 512 × 512-pixel or 256 × 256-pixel sub-frames to improve the efficiency of data reception. This will also allow to shorten the intervals of image acquisition, so that the reliability of cloud motion vectors may improve.

Table 4 Expected performance at Venus for $T_{SNS} = 65$ and 60 K

Wavelength (μm)	Flux (W cm^{-2} str^{-1} μ m^{-1})	Exp. (s)	Electrons (10^4 e^-)	S/N ratio	
				65 K	60 K
1.735	1.2×10^{-5}	6	7.7	250	280
2.260	1.6×10^{-5}	6	9.3	280	300
2.320	4.0×10^{-6}	10	3.1	125	170
2.020	2.2×10^{-4}	6	11	310	330

The "far" distance range (0.3–0.4 million km)

The 167-h (or 7-Earth-day) duration in this distance range should allow IR2 and other cameras to record a full rotation of the Venus atmosphere every orbit. Obtaining a series of global coverage, moderate spatial-resolution (~80 km per pixel), and long-time coverage data in the NIR windows and at 2.02 μm would be of great help to statistical studies of clouds.

Signal-to-noise ratio and science output

Expected signal-to-noise ratios (SNRs) for Venus observations are summarized in Table 4. The dark current of Eq. (4), the readout noise (constant 2 counts), and the shot noise of incoming photon are accounted for. We examine the effect of SNR on derived model parameters.

Effect of SNR on the cloud size parameters

Assuming the SNR for images are 200, we add 1 % to $I_{1.74\mu m}$ and subtract 1 % from $I_{2.3\mu m}$ (twice the standard deviation) in Eq. (3). While this changes m by 1.5 %, the obtained values for many pixels are statistically analyzed in a scatter plot (Carlson et al. 1993; Wilson et al. 2008). As 1.5 % errors may only slightly *blur* individual branches in the scatter plot (Carlson et al. 1993), they therefore have little effect on the identification of branches.

Effect of SNR on studies of sub-cloud CO

The CO absorption index curve for 30 ppmv (Fig. 3) is plotted with error bars corresponding to $I_{2.26\mu m} \pm 1\sigma$ and $I_{2.32\mu m} \pm 1\sigma$. By examining this, we anticipate to distinguish spatial inhomogeneity of CO of the order of 1 ppmv for cloud optical thicknesses $\tau \leq 25$, and 2 ppmv for $25 < \tau \leq 30$. As previous studies show CO variations of ~25 ppmv near the equator to ~40 ppmv at high latitudes (Taylor and Crisp 1997; Tsang et al. 2008), the CO absorption index as deduced from IR2 2.26- to 2.32-μm images will be a powerful tool to investigate the spatial inhomogeneities of CO in various scales.

Effect of SNR on cloud-top altimetry

An SNR greater than 300 is expected for 2.02-μm images; hence, it is possible to detect brightness variations of ~1 %. This will allow us to study a few mbar or ~100 m of pixel-to-pixel undulation of cloud top (Fig. 4).

Conclusions

IR2 onboard Akatsuki has been carefully designed, developed, and calibrated. The performance is assured by tests on the ground and is confirmed by in-flight observations after the launch (Satoh et al. 2015). As Akatsuki has successfully been inserted in the Venus orbit in December 2015 (Nakamura et al. 2016), IR2 will remain a unique instrument that can obtain NIR 1.74- and 2.3-μm window images of Venus from the orbit in the coming years.

Authors' contributions

All authors made valuable and selfless contribution to development, operation, and calibration of IR2. All authors read and approved the final manuscript.

Author details

[1] Institute of Space and Astronautical Science, Japan Aerospace Exploration Agency, 3-1-1 Yoshinodai, Chuo-ku, Sagamihara 252-5210, Japan. [2] Department of Space and Astronautical Science, School of Physical Sciences, SOKENDAI, 3-1-1 Yoshinodai, Chuo-ku, Sagamihara 252-5210, Japan. [3] National Astronomical Observatory of Japan, 2-21-1 Osawa, Mitaka 181-8588, Japan. [4] Tohoku University, 6-3 Aoba, Aramaki, Aoba-ku, Sendai 980-8578, Japan. [5] Sumitomo Heavy Industries, Ltd., 5-2 Sobirakicho, 792-0001 Niihama, Japan. [6] College of Science and Engineering, Ritsumeikan University, 1-1-1 Noji-higashi, Kusatsu 525-8577, Japan.

Acknowledgements

Scientific discussion with G. Hashimoto (Okayama U.), R. Nakamura (AIST), and M. Ishiguro (Seoul U.) was essential to define the science objectives and requirements to IR2. Special thanks go to the following companies: Nikon for design and manufacturing of IR2 optics; Magoshi for the high-performance baffle; MELCO for the unique PtSi sensor; Kyocera, Corp. for space-quality package for PtSi; Fujitoku, Corp. for interfacing with Barr Associates, Inc., the filter manufacturer.

Competing interests

The authors declare that they have no competing interests.

Received: 5 November 2015 Accepted: 18 April 2016
Published online: 04 May 2016

References

Akiyama A et al (1994) 1040 × 1040 infrared charge sweep device imager with PtSi Schottky-barrier detectors. Opt Eng 33:64–71

Allen D, Crawford J (1984) Cloud structure on the dark side of Venus. Nature 307:222–224

Carlson RW et al (1993) Variations in Venus cloud particle properties: a new view of Venus's cloud morphology as observed by the Galileo near-infrared mapping spectrometer. Planet Space Sci 41:477–485
Drossart P et al (2007) A dynamic upper atmosphere of Venus as revealed by VIRTIS on Venus Express. Nature 450:641–645
Esposito LW, Knollenberg RG, Marov MY, Toon OB, Turco RP (1983) The clouds and hazes of Venus. In: Hunten DM et al (eds) Venus. University of Arizona Press, Arizona, pp 484–564
Fukuhara T et al (2011) LIR: Longwave infrared camera onboard the Venus orbiter Akatsuki. Earth Planets Space 63:1009–1018
Grassi D et al (2014) The Venus nighttime atmosphere as observed by the VIRTIS-M instrument. Average fields from the complete infrared data set. J Geophys Res 119:837–849. doi:10.1002/2013JE004586
Grinspoon DH et al (1993) Probing Venus's cloud structure with Galileo NIMS. Planet Space Sci 41:515–542
Hasebe N et al (2008) Gamma-ray spectrometer (GRS) for lunar polar orbiter SELENE. Earth Planets Space 60:299–312
Haus R, Kappel D, Arnold G (2014) Atmospheric thermal structure and cloud features in the southern hemisphere of Venus as retrieved from VIRTIS/VEX radiation measurements. Icarus 232:232–248. doi:10.1016/j.icarus.2014.01.020
Ignatiev N et al (2009) Altimetry of the Venus cloud top from the Venus Express observations. J Geophys Res. doi:10.1029/2008JE003320
Iwagami N et al (2011) Science requirements and description of the 1 μm camera onboard the Akatsuki Venus Orbiter. Earth Planets Space 63:487–492
Kamp LW, Taylor FW (1990) Radiative-transfer models of the night side of Venus. Icarus 86:510–529
Khatuntsev IV et al (2013) Cloud level winds from the Venus Express Monitoring Camera imaging. Icarus 226:140–158
Knollenberg RG, Hunten DM (1980) Microphysics of the clouds of Venus: results of the Pioneer Venus particle size spectrometer experiment. J Geophys Res 85:8039–8058
Kouyama T, Imamura T, Nakamura M, Satoh T, Futaana Y (2013) Long-term variation in the cloud-tracked zonal velocities at the cloud top of Venus deduced from Venus Express VMC images. J Geophys Res 118:37–46. doi:10.1029/2011JE004013
Matsumoto T, Kawada M, Murakami H, Noda M, Matsuura S, Tanaka M, Narita K (1996) IRTS observation of the near-infrared spectrum of the zodiacal light. Publ Astron Soc Jpn 48:47–51
Moissl R et al (2009) Venus cloud top winds from tracking UV features in Venus Monitoring Camera images. J Geophys Res. doi:10.1029/2008JE003117
Nakamura M et al (2011) Overview of Venus orbiter, Akatsuki. Earth Planets Space 63:443–457
Nakamura M et al (2014) Return to Venus of the Japanese Venus climate orbiter AKATSUKI. Acta Astronaut 93:384–389. doi:10.1016/j.actaastro.2013.07.027
Nakamura M et al (2016) AKATSUKI returns to Venus. Earth Planets Space (accepted)
Patsaeva MV et al (2015) The relationship between mesoscale circulation and cloud morphology at the upper cloud level of Venus from VMC/Venus Express. Planet Space Sci 113–114:100–108. doi:10.1016/j.pss.2015.01.013
Peralta J et al (2008) Characterization of mesoscale gravity waves in the upper and lower clouds of Venus from VEX-VIRTIS images. J Geophys Res. doi:10.1029/2008JE003185
Piccioni G et al (2007) South-polar features on Venus similar to those near the north pole. Nature 450:637–640
Sato TM et al (2014) Cloud top structure of Venus revealed by Subaru/COMICS mid-infrared images. Icarus 243:386–399. doi:10.1016/j.icarus.2014.09.004
Satoh T et al (2009) Cloud structure in Venus middle-to-lower atmosphere as inferred from VEX/VIRTIS 1.74 μm data. J Geophys Res. doi:10.1029/2008JE003184
Satoh T et al (2015) Venus' clouds as inferred from the phase curves acquired by IR1 and IR2 on board Akatsuki. Icarus 248:213–220. doi:10.1016/j.icarus.2014.10.030
Schubert G (1983) General circulation and the dynamical state of the Venus atmosphere. In: Hunten DM et al (eds) Venus. University of Arizona Press, Arizona, pp 681–765
Stauffer JR et al (2007) Near- and mid-infrared photometry of the Pleiades and a new list of substellar candidate members. Astrophys J Suppl 172:663–685
Svedhem H, Titov D, Taylor F, Witasse O (2009) Venus Express mission. J Geophys Res. doi:10.1029/2008JE003184
Sánchez-Lavega A et al (2008) Variable winds on Venus mapped in three dimensions. Geophys Res Lett. doi:10.1029/2008GL033817
Taylor FW, Crisp D (1997) near-infrared sounding of the lower atmosphere of venus. In: Bougher SW, Hunten DM, Phillips RJ (eds) Venus II: geology, geophysics, atmosphere, and solar wind environment. University of Arizona Press, Tucson, pp 325–351
Titov DV et al (2009) Venus Express: highlights of the nominal mission. Sol Syst Res 43:185–209. doi:10.1134/S0038094609030010
Tsang CCC et al (2008) Tropospheric carbon monoxide concentrations and variability on Venus from Venus Express/VIRTIS-M observations. J Geophys Res. doi:10.1029/2008JE003089
von Zahn U, Kumar S, Niemann H, Prin R (1983) Composition of the Venus atmosphere. In: Hunten DM et al (eds) Venus. University of Arizona Press, Arizona, pp 299–430
Wilson CF et al (2008) Evidence for anomalous cloud particles at the poles of Venus. J Geophys Res. doi:10.1029/2008JE003108
Yung YL et al (2009) Evidence for carbonyl sulfide (OCS) conversion to CO in the lower atmosphere of Venus. J Geophys Res. doi:10.1029/2008JE003094